

08,09,12

Structure Analysis, Photoluminescence, and Non-linear/Linear Optical Parameters of $\text{Li}_2\text{Ge}_4\text{O}_9:\text{Mn}^{4+}$ Transparent Glass-Ceramic

© I. Morad^{1,2}, X. Liu³, H. Elhosiny Ali^{4,5,*}, M.M. El-Desoky², J. Qiu¹

¹ State Key Laboratory of Modern Optical Instrumentation, College of Optical Science and Engineering, Zhejiang University, Hangzhou 310027, China

² Department of Physics, Faculty of Science, Suez University, Suez, Egypt

³ School of Materials Science and Engineering, Zhejiang University, Hangzhou 310027, China

⁴ Research Center for Advanced Materials Science (RCAMS), King Khalid University, Abha 61413, P.O. Box 9004, Saudi Arabia

⁵ Department of Physics, Faculty of Science, Zagazig University, Zagazig, Egypt

* E-mail: hithamph@gmail.com

Received: January 18, 2022

Revised: January 26, 2022

Accepted: January 27, 2022

In this study, $\text{Li}_2\text{Ge}_4\text{O}_9:\text{Mn}^{4+}$ transparent glass-ceramic was prepared by conventional melt-quenching. The thermal treatment was used for the devitrification of the sample. The creation of a $\text{Li}_2\text{Ge}_4\text{O}_9$ nanocrystalline precipitated through the glass matrix was verified by X-ray diffraction and HR-TEM. Electron paramagnetic resonance spectra were employed to confirm the oxidation of Mn^{2+} to Mn^{4+} in glass-ceramic after thermal treatment. The photoluminescence spectra displayed a narrow red band centered at 668 nm ascribed to the spin-forbidden ${}^4E_g \rightarrow {}^4A_{2g}$ transition of Mn^{4+} . To estimate the optical parameters, UV-Vis-IR absorption spectroscopies were measured. The red shift of the direct optical band gap E_g^{opt} , from 3.81 to 2.55 eV, was observed by increasing the Mn^{4+} concentration. The dispersion parameters, refraction indices (n , n_∞), and oscillator wavelength (λ_0) were examined by using Wemple–DiDomenico single-oscillator model. The relationship between the refractive index and the energy gap has been investigated using various models such as Moss, Hervé–Vandamme, Ravindra, and Singh–Kumar. In addition, the linear and non-linear optical properties of $\text{Li}_2\text{Ge}_4\text{O}_9:\text{Mn}^{4+}$ were mentioned. The temperature-dependent luminescence intensity measurement was also carried out. The method of preparation exposed herein for the synthesis of Mn^{4+} -doped GCs might be prevailing to produce identical luminescent ceramics in accordance with the glass's devitrification.

Keywords: glass-ceramics, photoluminescence, optical properties, non-linear/linear optical, dispersion parameters, energy gap

DOI: 10.21883/PSS.2022.06.54372.002

1. Introduction

The rising index of color rendering combined with a broad color gamut has been a constant research direction in display technologies and solid-state lighting, which has caused continuous potential in the phosphor materials progression providing narrow blue, red, and green emissions of high efficiency. Conventional rare-earth ions doped phosphor with red emission, *i.e.*, Eu^{3+} (or Eu^{2+}) has faced challenges associated with excitation/emission bandwidth, reabsorption, and efficiency. Therefore, the RE-free phosphors activated with many transition metals (TM) ions have received growing interest in recent years [1–5]. Among TM ions, Mn^{4+} with a $3d^3$ electron configuration gives strong red emission in a range of hosts, and Mn^{4+} phosphors including oxide and fluoride have been extensively exploited [6–9]. From a practical application point of view, the use of Mn^{4+} -activated oxides is preferred considering their

eco-friendly procedure of preparation and excellent chemical stability [10–13]. Concerning the optical features of red-emitting Mn^{4+} -doped phosphors, they show a sharp host-dependent emission peaking in the range of 620–700 nm, while do not exhibit any absorption in the green and blue spectral range, which is a particular advantage for solid-state lighting applications [14, 15]. These benefits, therefore, have triggered an increasing number of investigations into the synthesis as well as the spectroscopic properties belonging to red-emitting Mn^{4+} -doped phosphors. Recently, our research group has studied the tunable emission based on the Mn^{2+} coordination state variation from octahedral to tetrahedral through the precipitated $\alpha\text{-Zn}_2\text{SiO}_4$ crystals on glass surfaces [16]. Y. Takahashi *et al.* investigated crystallization and structural ordering in glassy ferroelectric $\text{Li}_2\text{Ge}_4\text{O}_9$ [17]. Moreover, Kunitomo *et al.* identified a dilithium tetragermanate ($\text{Li}_2\text{Ge}_4\text{O}_9$) paraelectric and ferroelectric host with red emission for Mn^{4+} [18], and

Suzuki *et al.* later showed that the quenching temperature for the Mn^{4+} emission could be improved by Na substitution in $\text{Li}(\text{LiNa})\text{Ge}_4\text{O}_9$ [1]. The Mn site occupancy in $\text{Li}_2\text{Ge}_4\text{O}_9 : \text{Mn}$ crystals were eventually illustrated according to the optical spectroscopy and structural analysis [19]. In comparison, synthesis of Mn^{4+} activated oxide and fluoride phosphors remains a major challenge as the Mn ions are usually stabilized in an oxidation state of +2 in most wet chemistry processes and solid-state reactions, and special precautions are needed to regulate the high-yield oxidation of Mn ions to Mn^{4+} .

Herein, a synthetic technique for Mn^{4+} -doped $\text{Li}_2\text{Ge}_4\text{O}_9$ glass-ceramic (GC) was fabricated by a conventional melt-quenching performance. The electron paramagnetic spectroscopy and optical spectroscopy were studied. The optical properties of the Mn^{4+} -doped $\text{Li}_2\text{Ge}_4\text{O}_9$ GC have been investigated. The model of a single oscillator reported by Wemple–DiDomenico was used to calculate the dispersion variables (E_0 and E_d). Also, the non-linear parameters have been deduced.

2. Experimental

The melt-quenching method has been used to prepare the glass samples with the compositions of $80\text{GeO}_2 - 20\text{Li}_2\text{O} - x\text{MnO}_2$ ($x = 0.1, 0.3, 0.5, 0.7, 1.0, 1.5 \text{ mol.}\%$). The commercially available oxide powders Li_2CO_3 , GeO_2 , and MnO_2 were applied as raw materials. All precursor oxides were mixed thoroughly and crushed in ethanol, and then annealed at 500°C in a muffle furnace for at least 3 hours before synthesis to remove adsorbed water. In a typical procedure, raw materials with a weight of 20 g were thoroughly mixed manually. To extract the CO_2 , the powder was initially heated for 4 hours at 600°C followed by melting inside a covered alumina crucible under air for 45 min. at 1200°C . The melt of the glass is then cast onto a stainless-steel plate. At 400°C (*i.e.*, around $\sim 90^\circ\text{C}$ beneath the glass transition temperature T_g given in DSC), the procured glasses were annealed for 60 min. to relieve the inner stress created by the quenching action and then cooled to room temperature (RT) naturally. All the produced glass samples were thermally treated under argon gas at 570°C for 60 min. with a $10^\circ\text{C} \cdot \text{min}^{-1}$ rate followed by cooling down to RT to efficiently yield transparent GC samples. G- x and GC- x labels denote glass and glass-ceramic which are often employed in the following discussion, where x corresponds to the concentration of Mn in mol percentage. For optical investigations, all the prepared G and GCs samples were smoothly polished with an area of $10 \text{ mm} \times 10 \text{ mm}$ and a thickness of 1.5 mm.

T_g and the crystallization temperature T_c were estimated by the assistance of the DTA curve (Fig. 1) recorded through the airflow at a $10^\circ\text{C}/\text{min}$. heating rate with a range of temperature from $20 - 1200^\circ\text{C}$. X-ray diffraction (XRD) is an effective way often utilized to distinguish the existence of the amorphous and crystalline phases in the G-samples in a

significant way and to recognize the structural properties of the prepared oxide glass and the crystallite phase produced in the glass samples' interior. The measurement was carried out using the $\text{CuK}\alpha$ radiation ($\lambda = 1.5418 \text{ \AA}$) XPERT-PRO-PANalytical-Netherland system at a $2^\circ/\text{min}$. rate in 2θ step sizes over a value ranging of $20 - 80^\circ$. In addition, the density of a glass-ceramic sample with different Mn^{4+} contents is measured by the Archimedes method using toluene as displacing medium. Energy dispersive X-ray (EDX) maps together with the scanning transmission electron microscopy (STEM) was used to determine the composition of the created GCs running a JEOL JEM-2100F TEM system running at a 200-kV accelerating voltage. A Lambda 900 spectrophotometer (PerkinElmer, USA) was used to measure the absorption spectra in a range between 200 and 800 nm as a function of wavelength. All measurements were performed at RT by placing the G and GCs samples. Using an (HR 800, Jobin-Yvon, France) Raman spectrometer working with an argon laser with 514.5-nm wavelength as an excitation source, the molecular structure of fabricated oxide glass and glass-ceramic was examined. A Bruker A30 EPR spectrometer (300 K, 9.866 GHz, X-band) was used to achieve the electron paramagnetic resonance (EPR) spectra at RT for the different Mn ions oxidation states analysis and their coordination environments. Photoluminescence (PL) and PLE were collected through an FLS920 fluorescence spectrometer (Edinburgh Instruments Ltd, UK) with an excitation source of a 450-W Xe lamp (Xe-900).

3. Results and discussion

3.1. Thermal and structure analysis

The glass powder DTA curve is illustrated in Fig. 1. Two exothermic peaks were observed at 495 and 588.66°C , which might be attributed to T_g and T_{c1} , respectively. Moreover, two additional crystallization peaks at 622°C and 675°C are assigned to T_{c2} and T_{c3} , respectively. This given

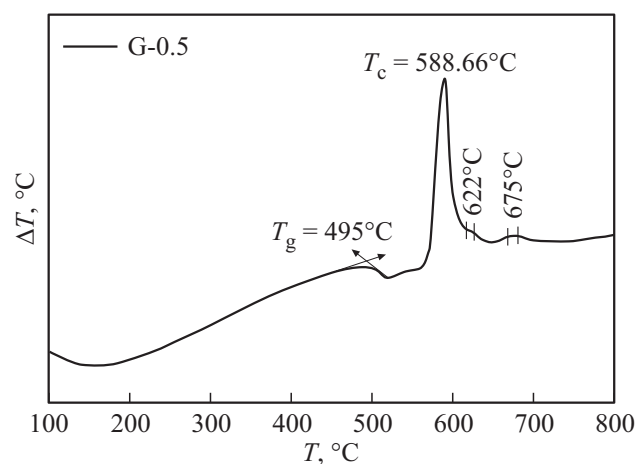


Figure 1. DTA graph for glass powder.

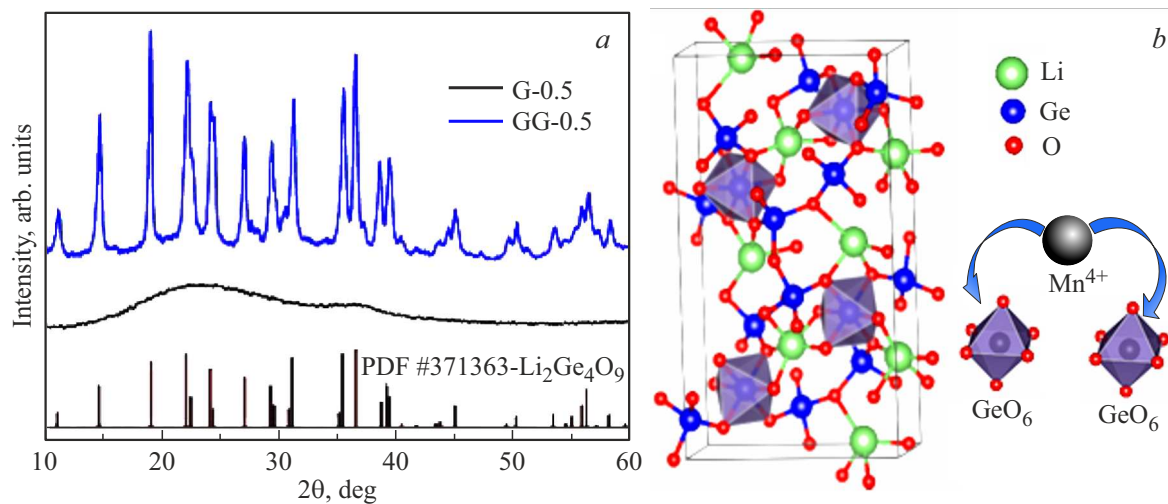


Figure 2. (a) XRD patterns of the G-0.5 and the thermal treatment GC-0.5 samples for 1 hour at 570°C. The JCPDS #37-1363 for $\text{Li}_2\text{Ge}_4\text{O}_9$ is presented in a reference. (b) Crystal structure of LiGe_4O_9 consisting of the $\text{GeO}_4/\text{GeO}_6$ units and lithium ions.

result is in good agreement with the result presented by Y. Takahashi *et al.* [17]. In general terms, the thermal stability and glass-forming ability are based on the temperature difference $\Delta T = T_c - T_g$ [21]. The value of ΔT approaches 95°C, indicating the high thermal stability of the prepared glass. The glass microstructure and the $\text{Li}_2\text{Ge}_4\text{O}_9-0.5\text{Mn}^{4+}$ GCs samples were examined using the XRD technique. As presented in Fig. 2, a, the absence of any diffraction peaks and the domination of two broad humps suggest the dominance of the glassy phase on the as-prepared glass sample. Contrariwise, after 570°C thermal treatment for 1 hour, there is a development of sharp diffraction peaks overlying upon the amorphous hump, as revealed in Fig. 2, a. These peaks can be assigned to $\text{Li}_2\text{Ge}_4\text{O}_9:0.5\text{Mn}^{4+}$ identified as JCPDS #37-1363 [18]. The estimated values of the crystallite size D using Scherrer's empirical formula [16, 22] are about 19.22 ± 1 nm. Crystallite size's value is small enough just to eliminate the dispersion resulting from the difference between crystallites and glass-matrix in refractive indices, therefore, the resultant GC shows relatively good transparency in the visible range [23].

The defect quantity of the sample could be expressed by the dislocation density labeled by δ . The density of dislocation represented the linear calculation of the crystal dislocation lines per unit volume. The δ is presented as a function of crystallite size D and presented by [24]:

$$\delta = \frac{1}{D^2}. \quad (1)$$

The dislocation density value δ for the thermally treated $\text{Li}_2\text{Ge}_4\text{O}_9-0.5\text{Mn}^{4+}$ GCs sample has been estimated to be 2.71 nm^{-2} .

The Scherrer evaluation just considered the crystallite size impact on XRD peak widening. The contribution from the lattice microstructures is not included, *i.e.*, the intrinsic strain in nanocrystals arising from the point defect, doping

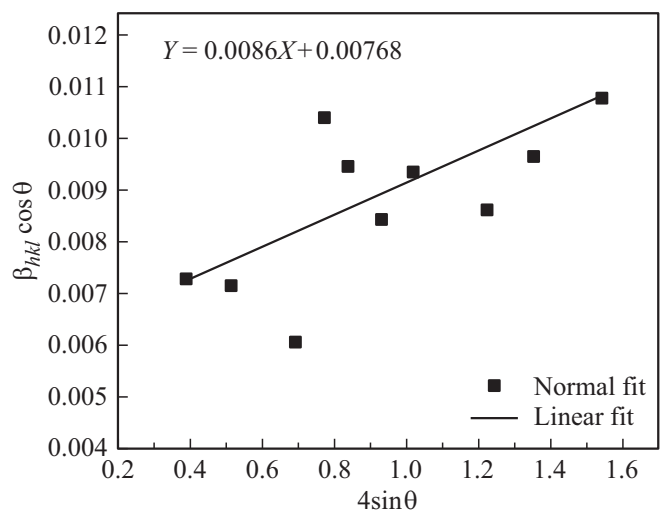


Figure 3. $\beta_{hkl} \cos \theta$ versus $4 \sin \theta$ of LiGe_4O_9 GC-0.5 Mn^{4+} sample.

of foreign atoms, stacking faults, grain boundary, and triple junction. According to Williamson–Hall approach, because of the coherent scattering area's limited size and the sample internal stress, the line expansion is analyzed. In this regard, the broadening of the diffraction line is related to the grain size together with the strain influence [25]. It could describe the lattice strain-induced broadening by [26]

$$\varepsilon = \frac{\beta_{hkl}}{4 \tan \theta}. \quad (2)$$

The lattice strain value of the $\text{Li}_2\text{Ge}_4\text{O}_9-0.5\text{Mn}^{4+}$ GCs was estimated to be 9.69. Moreover, the crystal size could also be computed by applying the Williamson–Hall approach given by Eq. (3) [27]:

$$\beta_{hkl} \cos \theta_{hkl} = 4\varepsilon \sin \theta_{hkl} + \frac{K\lambda}{D} \quad (3)$$

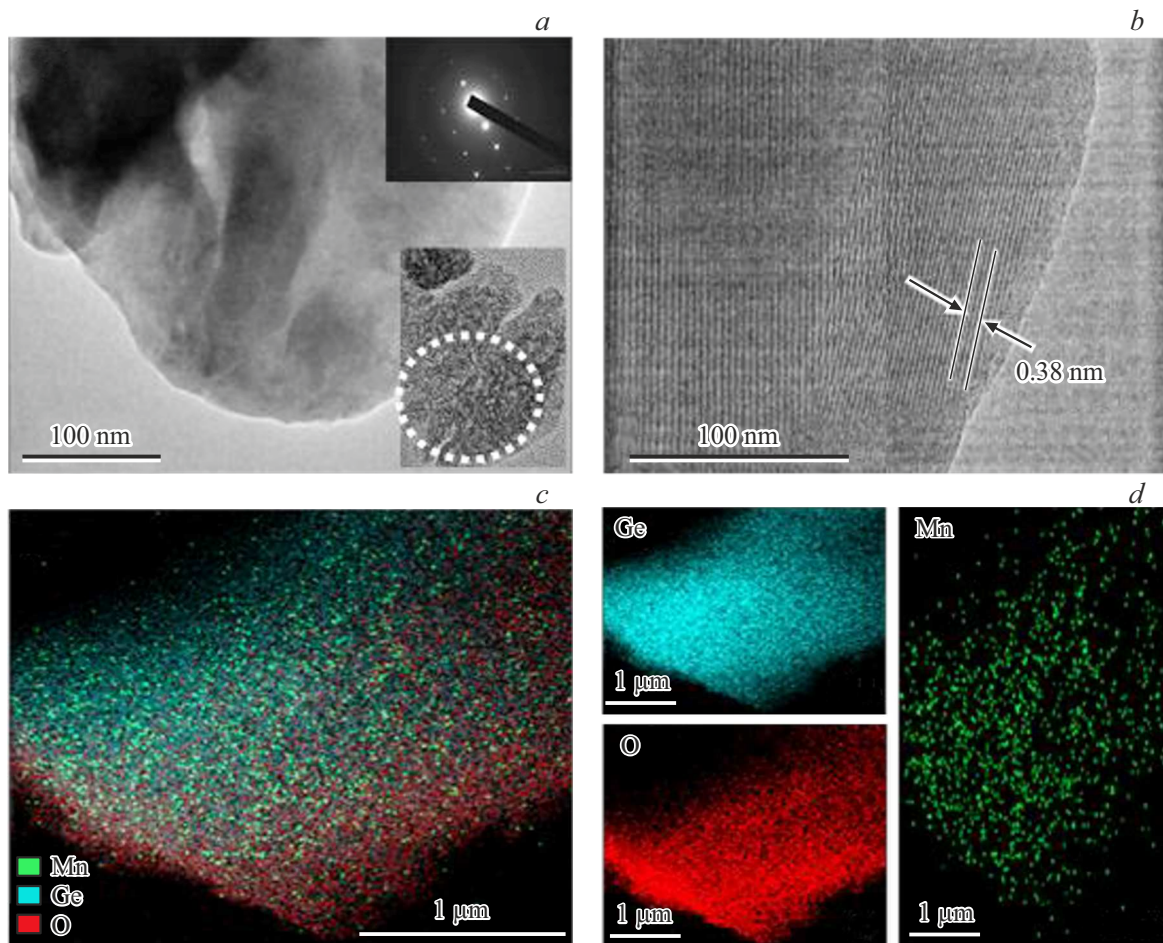


Figure 4. (a, b) HR-TEM and SAED. (c) EDX of GC-0.5. (d) Ge, O, and Mn elemental distributions.

and after the linear fitting, the crystalline size is derived from the y -intercept; in contrast, the lattice strain ε is employed by the fitting slope as shown in Fig. 3, the derived lattice strain and crystallite size values are 8.61 and 18.05 nm, respectively. By comparing these values with the values calculated using the Scherrer analysis, it is found that there is a perfect matching between them.

The crystal structure of $\text{Li}_2\text{Ge}_4\text{O}_9$ is described in Fig. 2, b. The $\text{Li}_2\text{Ge}_4\text{O}_9$ crystal has an orthorhombic structure in which GeO_4 tetrahedrons are joined by GeO_6 octahedrons to create a three-dimension framework. Besides, monovalent Li^+ cation is situated as part of the structural hollows created by the Ge–O polyhedral framework [28,29]. STEM and SAED images of $\text{Li}_2\text{Ge}_4\text{O}_9-0.5\text{Mn}^{4+}$ GCs are illustrated in Fig. 4, a. It is noticeable that the STEM image reveals that the examined GCs sample is relatively homogeneous; nevertheless, a closer look reveals the presence of porous structure with pore size around 0.3 nm (inset of Fig. 4, a).

The SAED pattern (Fig. 4, a inset) shows clear evidence of the crystalline phase, and the pattern can be unambiguously assigned to $\text{Li}_2\text{Ge}_4\text{O}_9$ nanocrystals. An interplanar space of 0.38 nm is revealed by the HRTEM image,

which can be attributed to the $\text{Li}_2\text{Ge}_4\text{O}_9$ (202) crystal plane ($d_{(202)} = 0.38$ nm). Additionally, the STEM-EDX element mappings of GC-0.5 presented in Fig. 4, inset c evidence the Ge, O, and Mn elements homogeneous distribution, verifying the Mn incorporation onto the GC-0.1 crystalline phase. EPR spectra of G-0.5 and $\text{Li}_2\text{Ge}_4\text{O}_9-0.5\text{Mn}^{4+}$ GCs samples have been illustrated to confirm the stabilization of Mn^{4+} through the GCs sample after heat treatment as displayed in Fig. 5, b. In the EPR spectrum, a clear-resolved sextet as a result of spin quantum number $M_s = |-1/2\rangle \rightarrow |+1/2\rangle$ is illustrated by the EPR spectrum of G-0.5, superimposed on broadband caused by the manganese ions electron spin hyperfine interaction with their particular $I = 5/2$ Mn nuclear spin, moreover, the estimated g -value is 2.026, and this isotropic signal is owing to Mn^{2+} in the octahedral symmetry environment [30,31]. On the contrary, according to the EPR spectra of the GC sample, the sextet resolved hyperfine lines at around 150 mT are observed, which corresponds to the forbidden transitions of Mn^{4+} [32]. The evaluated g -value is around 1.98 for Mn^{4+} ($3d^3$, $S = 3/2$). The same EPR spectrum of Mn^{4+} has been reported for different hosts [31–34].

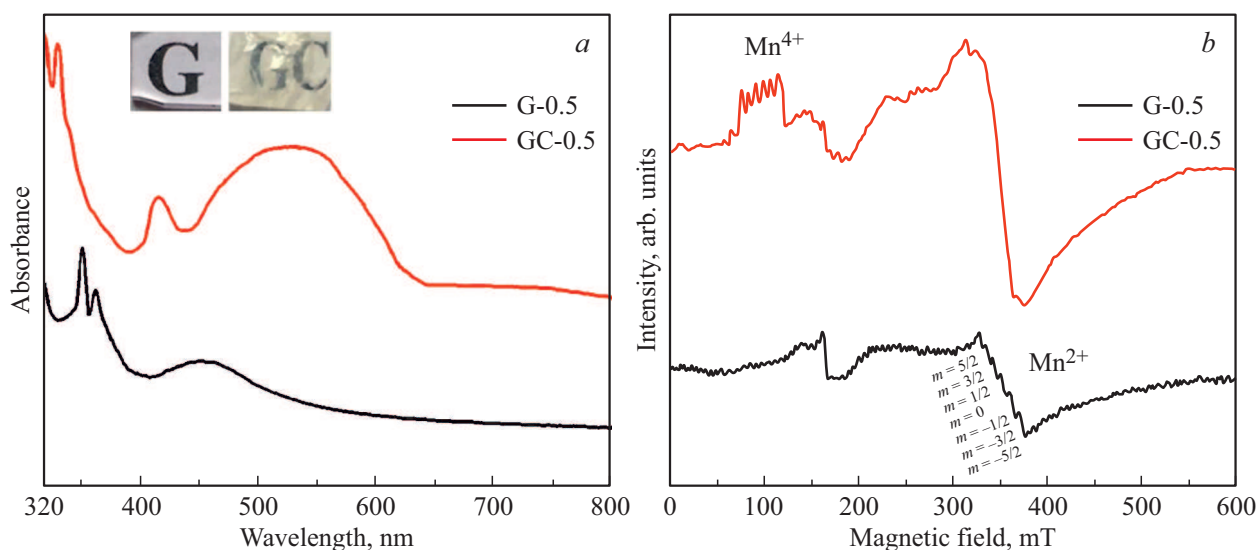


Figure 5. (a) Absorption spectrum of G-0.5 and GC-0.5. The inset is the photograph of the samples. (b) EPR spectra of G-0.5 and GC-0.5.

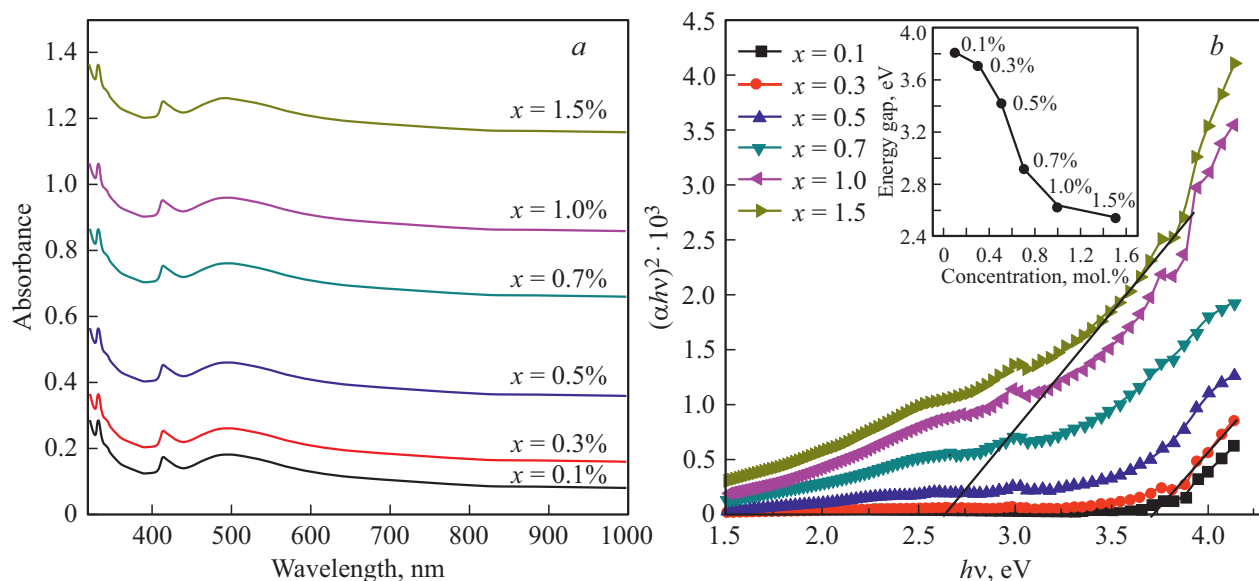


Figure 6. (a) Absorption spectra of $\text{Li}_2\text{Ge}_4\text{O}_9$ GC samples with different Mn^{4+} concentrations. (b) The relation between $(h\nu)$ and $(ah\nu)^2$ for $\text{Li}_2\text{Ge}_4\text{O}_9-x \text{Mn}^{4+}$ GCs samples (x is the Mn^{4+} concentrations).

3.2. Optical properties

To investigate the GCs samples' optical properties, we examined the absorption spectrum first of $\text{Li}_2\text{Ge}_4\text{O}_9$ GCs samples with different Mn^{4+} contents. As presented in Fig. 6, a, the absorption spectra represent a 417-nm absorption band beside another one centered at 332 nm owing to the electronic transition ${}^4\text{A}_{2g} \rightarrow {}^4\text{T}_{2g}$ and ${}^4\text{A}_{2g} \rightarrow {}^4\text{T}_{1g}$ of Mn^{4+} . The strong and broad absorption band extends from 400 to 700 nm attributed to the charge transfer excitation of the $\text{Mn}^{4+}-\text{O}$ complex [35]. Moreover, for comparison, we have demonstrated the absorption spectrum for the G-0.5 sample and presented it in Fig. 5, a. The spectrum

shows two 451- and 372-nm absorption bands; these bands may be corresponding to the Mn^{2+} electronic transition ${}^6\text{A}_{1g}(s) \rightarrow {}^4\text{E}_{1g}(D)$ and ${}^6\text{A}_{1g}(S) \rightarrow {}^4\text{A}_{1g}(G)$, ${}^4\text{E}_g(G)$, respectively, besides the charge-transfer absorption that presented by 351-nm band [36, 37].

Nevertheless, the Mn^{4+} doping $\text{Li}_2\text{Ge}_4\text{O}_9$ absorption intensity increases with the rise of Mn^{4+} concentrations accompanied by the absence of any change in the absorption edge as shown in Fig. 6, a. Furthermore, the spectrum of absorption is believed to be an important tool for deducing the optical band gap E_g^{opt} . The law of Tauc, Eq. (4), is often utilized for E_g^{opt} evaluation based on the absorption

Table 1. Dispersion parameters, S_0 , λ_0 , N/m^* , n_∞ , and n_∞ of the $\text{Li}_2\text{Ge}_4\text{O}_9-x\text{Mn}^{4+}$ GCs.

Mn^{4+} contents x	Density ± 0.01 , g/cm^3	E_g^{opt}	E_g^{W} , eV	E_U	E_d , eV	E_0	n	S_0 , $10^{13} \cdot \text{m}^{-2}$	N/m^* , $10^{56} \cdot \text{m}^{-3}$	n_∞	ϵ_s
0.1	2.82	3.81	3.87	0.21	6.87	4.54	1.669	1.373	1.547	1.955	4.429
0.3	2.91	3.71	3.62	0.25	7.11	4.39	1.622	8.238	2.423	2.230	4.960
0.5	2.94	3.42	3.3	0.27	9.58	4.23	1.862	1.181	2.826	2.458	6.040
0.7	3.21	2.91	3.1	0.28	15.27	3.93	2.218	2.348	3.031	2.728	7.444
0.1	3.8	2.63	2.79	0.30	19.16	3.73	2.367	3.606	3.578	2.757	7.605
1.5	4.09	2.55	2.79	0.31	28.02	3.67	2.853	7.000	3.949	3.222	11.341

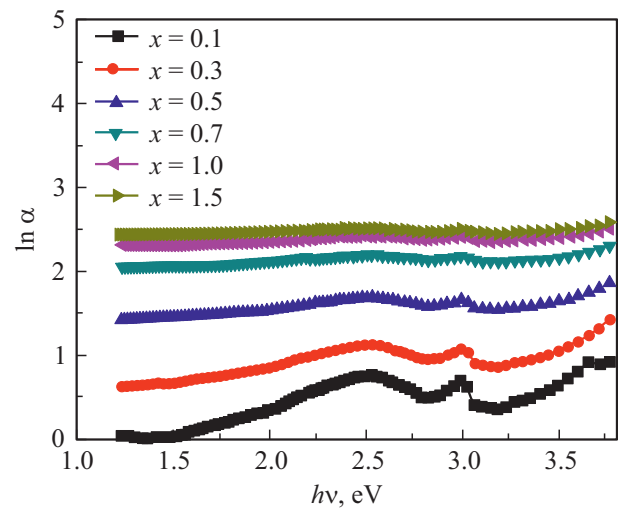
spectrum [38].

$$\alpha h\nu = A(h\nu - E_g^{\text{opt}})^n, \quad (4)$$

where $h\nu$ represents the photon energy, the arbitrary constant A relies on the internal transition band, and n symbolizes the index that identifies the electronic transitions leading to optical absorption. In the indirect optical transitions, n assumes the 2-value or 1/2 for direct permitted optical transitions. Fig. 6, *b* demonstrates a plot graph between $(\alpha h\nu)^2$ and $(h\nu)$, and hence to derive the optical energy gap (E_g^{opt}) can be acquired for direct transitions by extrapolating $(\alpha h\nu)^2 = 0$, and the estimated values of the $\text{Li}_2\text{Ge}_4\text{O}_9$ GCs with different Mn^{4+} are tabulated in Table 1. The glass crystallization, as well as the increasing of the Mn^{4+} content from 0.1 to 1.5% of Mn^{4+} , the E_g^{opt} decreases from 3.87 to 2.79 eV. This is potentially due to the gap reduction between the conduction and valence band due to the Mn^{4+} incorporation, and the establishment of crystals that generate a localized electronic state through the forbidden gap permitting electronic transitions with minimal energy. This falling off resulted from the bond energy and the conduction band's level reduction, which might be proceeded from the creation of the non-bridging oxygen. In amorphous semiconductors, close to the absorption edge, there are three classes of optical transitions that typically explain optical absorption in terms of transitions among tail and tail states, tail and extended states, and extended and extended states. The first corresponding two classes are compatible with $\nu \leq E_g^{\text{opt}}$ and the third one corresponds to $\nu \geq E_g^{\text{opt}}$. Even though there are three distinct regions in the absorption coefficient α plot as opposed to photon energy $h\nu$. In the second zone, the absorption bands are corresponding with transitions to expanded states throughout the conduction band from the localized states upon the edge of the valence band and/or from large states below the conduction band in the localized states to the valence band. The coefficient of absorption spectral dependency is typically accepted as the so-called Urbach principle. Eq. (5) [39].

$$\alpha = \beta \exp\left(\frac{h\nu}{E_U}\right), \quad (5)$$

where E_U refers to the alleged Urbach energy that expresses the optical activation energy, which constitutes

**Figure 7.** Urbach plot, $\ln \alpha$ versus photon energy ($h\nu$) for $\text{Li}_2\text{Ge}_4\text{O}_9-x\text{Mn}^{4+}$ GCs samples.

the bandwidth of localized states in the forbidden band. Consequently, from plotting $\log \alpha$ versus photon energy $h\nu$ for $\text{Li}_2\text{Ge}_4\text{O}_9-x\text{Mn}^{4+}$ GCs, E_U could be deduced from the inverse of the slope fitting (Fig. 7) [40,41]. The Urbach energy values of the GCs samples doped with different Mn^{4+} contents are tabulated in Table 1. Because the Urbach energy of glass semiconductors implicitly determines the disorder level, so, the crystallization decreases the Urbach energy and the resulting order of this phase. Moreover, it was found that the Urbach energy increases with increasing the Mn^{4+} concentration in the GCs samples, and this increase may be assigned to the rise of disorder arising in the GCs that took place by Mn^{4+} additions. Besides, the rise of Mn^{4+} concentrations causes a redistribution for the states from band to tail, thus providing a superior amount of the possible band to take part in the tail and tail transitions.

One of the most significant criteria of a material that is essential for excessive utilization in optical systems is the refractive index n . The n -value for the GC samples can be assessed from the reflectance R and extinction coefficient K by exploiting the relationship provided in Eq. (6) [42].

$$n = \frac{(1+R)}{(1-R)} + \sqrt{\frac{4R}{(R-1)^2} - K^2}. \quad (6)$$

The n -value of $\text{Li}_2\text{Ge}_4\text{O}_9$ GCs samples with different Mn^{4+} ion concentrations based on the wavelength is presented in Fig. 8. The n -value increases from 1.669 to 2.853 at 600 nm with increasing the Mn^{4+} contents, this is due to the increase in the GCs density (Table 1). Indeed, the refraction will be strong as the incident light interacts with the material containing enormous particles, and hence the refractivity of the substance will also be raised.

The dispersion of the refractive index was examined utilizing the single oscillator based on Wemple and DiDomenico approach in normal dispersion (the transparent area). In their model, it is possible to describe the n -value upon a frequency (ν) concerning the dispersion energy E_d and single oscillator energy E_o , respectively, where E_o refers to computations of the electronic transition mean excitation energy and E_d denotes the average inter-band optical transitions strength [43].

$$n^2 - 1 = \frac{E_o E_d}{E^2 - (h\nu)^2}. \quad (7)$$

Both E_o and E_d quantities can be derived by illustrating $1/(n^2 - 1)$ against $(h\nu)^2$, depending on the estimated intercept and slope, as indicated in Fig. 9.

The estimated values of E_o and E_d are recorded in Table 1. It could be seen that the E_o values decline with increasing the Mn^{4+} ion concentration. This decrease might be assigned to the increase of the localized states through the energy gap which in return improves the small energy transitions and leads to a decline in the E_o value. It is common knowledge. E_d 's dispersion energy is highly dependent on changes in the structural order of substances [44]. From Eq. (9), the static refractive index n_o was estimated at zero energies, and afterward the static dielectric constant ϵ_s . Concerning the model of a single oscillator [45], the average oscillator strength S_o , the refractive index at low energy n_∞ , and wavelength of inter-band oscillator λ_o for the $\text{Li}_2\text{Ge}_4\text{O}_9-x\text{Mn}^{4+}$ GCs have been estimated. The S_o , λ_o , and n_∞ of various Mn^{4+} -doped $\text{Li}_2\text{Ge}_4\text{O}_9$ GCs samples are estimated by drawing the $1/(n^2 - 1)$ against $(1/\lambda^2)$, Fig. 10, and tabulated in Table 1.

To calculate the long-wavelength refractive index n_∞ , average inter-band oscillator of wavelength λ_o equation has been considered as [43, 46]

$$\frac{n_\infty^2 - 1}{n^2 - 1} = 1 - \left(\frac{\lambda_o}{\lambda}\right)^2. \quad (8)$$

The estimated n values can be extrapolated to acquire the values of ϵ_∞ . In conformity with Morad and Pankove [38, 46], the dielectric constant real part is described by

$$\epsilon' = n^2 - K^2 = \epsilon_\infty - \frac{e^2 N}{\pi \epsilon_0 m^* C^2} \lambda^2, \quad (9)$$

where N is the concentration of free charge-carrier. The ϵ' versus λ^2 exhibits a linear relation at lower energy, as

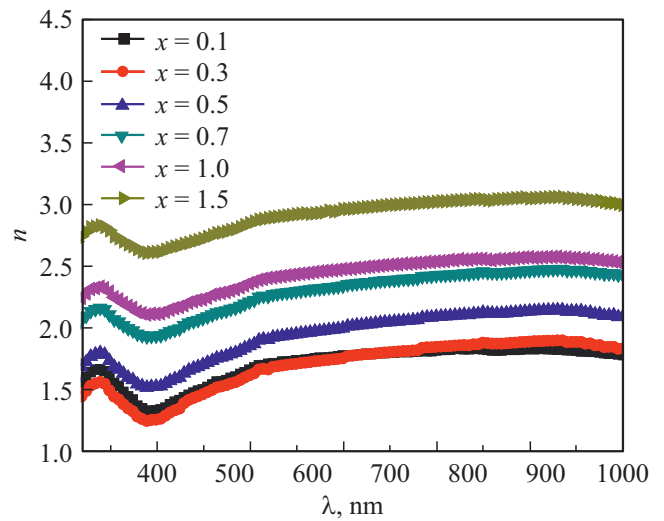


Figure 8. The dependence of refractive index on wavelength for $\text{Li}_2\text{Ge}_4\text{O}_9-x\text{Mn}^{4+}$ GCs.

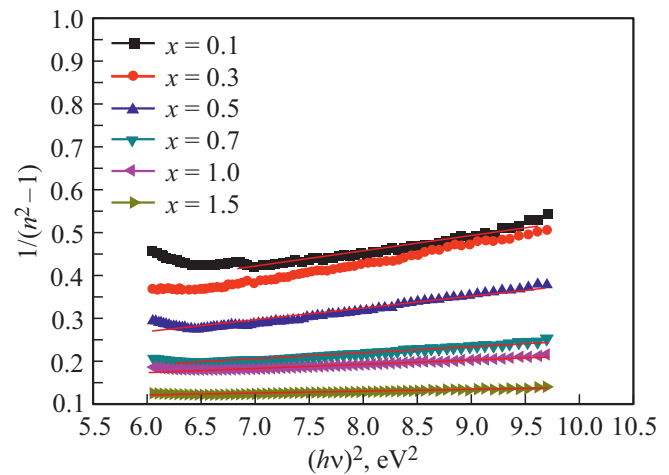


Figure 9. $1/(n^2 - 1)$ curves versus $h\nu^2$ for the $\text{Li}_2\text{Ge}_4\text{O}_9-x\text{Mn}^{4+}$ GCs.

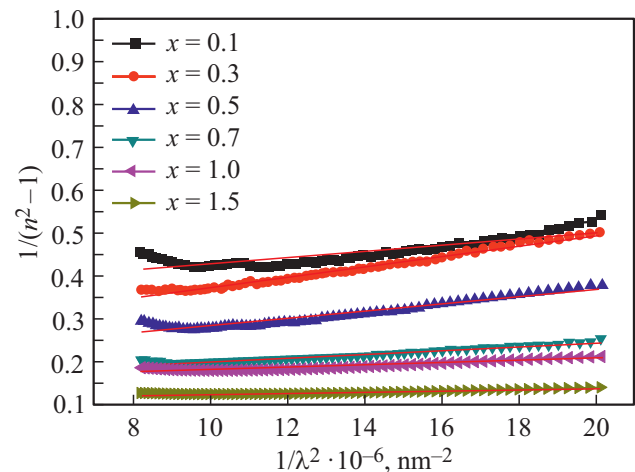


Figure 10. $1/(n^2 - 1)$ curves versus $1/\lambda^2$ for the $\text{Li}_2\text{Ge}_4\text{O}_9-x\text{Mn}^{4+}$ GCs.

Table 2. Non-linear and linear optical and dielectric variables of $\text{Li}_2\text{Ge}_4\text{O}_9-x\text{Mn}^{4+}$ GCs.

Mn^{4+} contents x	n_{HV}	n_{K}	n_{M}	n_{Rv}	n_{R}	n_{A}	ε_{∞}	ε_0	$\chi^{(1)}$, esu	$\chi^{(3)}$, 10^{-12} esu	$n^{(2)}$, 10^{-11}
0.1	2.135	2.188	2.235	2.307	2.254	2.638	5.257	63.157	0.339	2.243	3.686
0.3	2.158	2.206	2.250	2.323	2.281	2.658	5.348	54.359	0.346	2.442	3.979
0.5	2.231	2.265	2.296	2.371	2.362	2.716	5.633	33.977	0.369	3.147	4.996
0.7	2.376	2.386	2.390	2.468	2.524	2.818	6.219	13.582	0.415	5.066	7.655
0.1	2.467	2.465	2.452	2.531	2.625	2.874	6.600	8.772	0.446	6.717	9.852
1.5	2.495	2.490	2.471	2.551	2.656	2.89	6.719	8.021	0.455	7.305	10.619

illustrated in Fig. 11. The N/m^* and ε_{∞} can be evaluated by the slope and intercept of the curve linear portion, respectively. In addition, n_{∞} could be deliberated.

These evaluated values were illustrated in Table 1. It could be noted that the free carriers increase (N/m^*) together with the long-wavelength refractive index (n_{∞}) values rise with rising the Mn^{4+} concentration.

The refractive index n considers a significant fundamental aspect of glass and GCs materials and is related to the local field within the material. T.S. Moss [47] proposed a relationship connecting the refractive index with the energy gap, based on the notion that the energy levels in dielectric concept are rated as a parameter $(\varepsilon_{\infty})^2$ or n^4 , *i. e.*, is termed in the rates of dielectric energy theory.

$$n_{\text{M}}^4 E_{\text{g}} = 95 \text{ eV} \quad (10)$$

The evaluated refractive index values by Moss (n_{M}) increased gradually with rising the Mn^{4+} ion contents as tabulated in Table 2.

Ravindra *et al.* [48, 49] suggested a further linear correlation providing the n -value dependence and given by

$$n_{\text{Rv}} = 4.084 - 0.62E_{\text{g}}. \quad (11)$$

As illustrated in Table 2, there is an enhancement in the derived values of n_{Rv} with Mn^{4+} addition, the value rises from 2.251 to 2.551 for higher Mn^{4+} concentration. This indicates the clear effect of more Mn^{4+} addition in the $\text{Li}_2\text{Ge}_4\text{O}_9$ GCs.

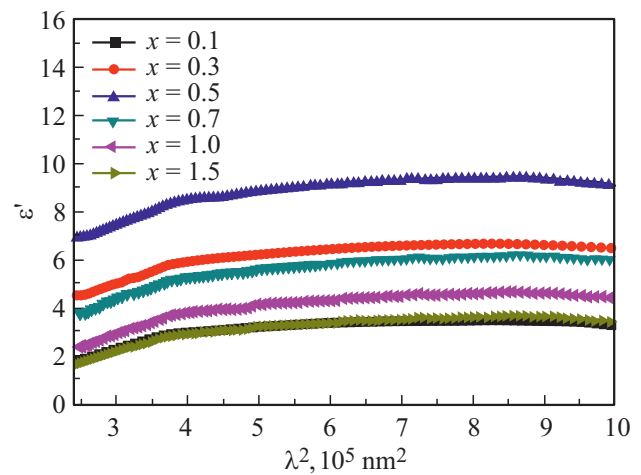
By a normal term subtracted from the energy gap, the Reddy partnership is comprehensive concerning the Moss relationship and exhibits identical conduct as the Moss relation. Reddy *et al.* recommended the subsequent relationship [50]:

$$n_{\text{R}}^4 (E_{\text{g}} - 0.365) = 154. \quad (12)$$

The derived n -value using this relation is provided in Table 2, as it intensified from 2.254 to 2.656 by rising the Mn^{4+} contents from 0.1 to 1.5%.

Anani's model presented by Eq. (12) makes the refractive-index evaluation easy to be achieved:

$$n_{\text{A}} = \frac{17 - E_{\text{g}}}{5}. \quad (13)$$

**Figure 11.** Relation between ε' and λ^2 for $\text{Li}_2\text{Ge}_4\text{O}_9-x\text{Mn}^{4+}$ GC.

The calculated values of n_{A} is illustrated in Table 2, where the n_{A} increases slightly by adding Mn^{4+} ion and also gradually enhances with adding more contents.

Predicated on the vibrations system, Hervé-Vandamme [51] displayed a relationship for the refractive index as presented in the following form.

$$n_{\text{HV}} = \sqrt{1 + \left(\frac{13.6 \text{ eV}}{E_{\text{g}} + 3.4 \text{ eV}} \right)^2}, \quad (14)$$

where the hydrogen ionizing energy denoted as 13.6 and 3.4 eV is believed to be the variance joining UV resonance energy and the band gap energy.

The calculated n_{M} and n_{HV} values were listed in Table 2. The dependence of these parameters on the Mn^{4+} contents is obvious, while they increase from 2.235 to 2.471 and from 2.135 to 2.495, respectively, with rising the Mn^{4+} ion contents from 0.1 to 1.5%.

Kumar and Singh have lately developed a series of parameters to establish an exponential relationship for refractive indexes for several experimental refractive indices and energy gaps [52].

$$n_{\text{K}} = KE_{\text{g}}^B, \quad (15)$$

where $K = 3.3668$ and $B = -0.32234$.

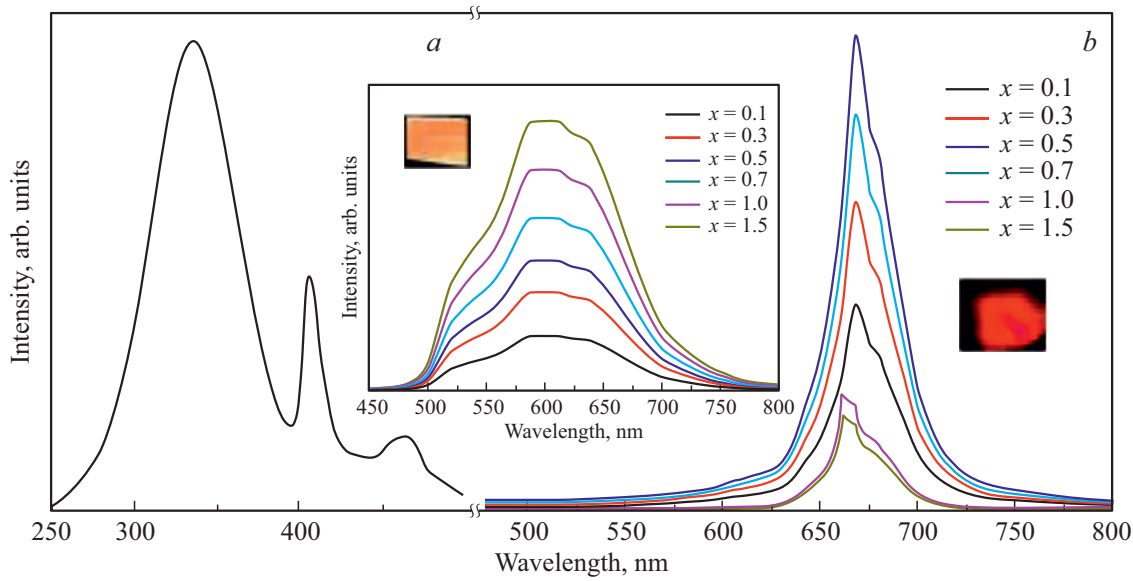


Figure 12. PL emission ($\lambda_{\text{ex}} = 325 \text{ nm}$) and PLE excitation ($\lambda_{\text{em}} = 668 \text{ nm}$) spectra of $\text{Li}_2\text{Ge}_4\text{O}_9-x\text{Mn}^{4+}$ GC samples. The inset is the emission spectra of G-xMn^{2+} .

The values of n_K varied from 2.188 for the lowest concentration (0.1%) to 2.49 for the higher concentration (1.5%) as illustrated in Table 2.

The various calculated refractive index values are set out in Table 2, the average n value labeled by n_{av} has been estimated via the following expression and listed in Table 2:

$$n_{\text{av}} = \frac{n_M + n_{Rv} + n_{HV} + n_R + n_A + n_K}{6}. \quad (16)$$

As long as a set of electron-device assets, the value of solids optical dielectric is essential. In the next formula, the static dielectric constants, as well as the high-frequency dielectric constants (ϵ_0 and ϵ_∞), were assigned as follows [53]:

Static dielectric constant

$$\epsilon_0 = -33.26876 + 78.61805E_g - 45.70795E_g^2 + 8.32449E_g^3. \quad (17)$$

High-frequency dielectric constant

$$\epsilon_\infty = n_{\text{av}}^2. \quad (18)$$

The estimated ϵ_0 and ϵ_∞ values of $\text{Li}_2\text{Ge}_4\text{O}_9-x\text{Mn}^{4+}$ GCs samples with different Mn^{4+} ion concentrations were introduced in Table 2.

3.3. Non-linear optical analysis of the $\text{Li}_2\text{Ge}_4\text{O}_9-x\text{Mn}^{4+}$ GCs

The non-linear optical performance emerges from the interaction of the high-intensity light with the substance's atomic oscillator. The GCs samples attempt to establish second and third harmonics if it is under high-intensity laser-like light interaction. Polarization functions as a linear response to the low intensities electric field, whereas non-linear is at high intensities.

The GCs materials with higher non-linearity possess various industrial applications, in particular communications, data storage, *etc.* [54, 55]. In terms of non-linear polarizability P_{NL} , the polarizability p is denoted by [56]:

$$p = \chi^{(1)}E + P_{\text{NL}}, \quad (19)$$

where $P_{\text{NL}} = \chi^{(2)}E^2 + \chi^{(3)}E^3$ and $\chi^{(1)}$, $\chi^{(2)}$, and $\chi^{(3)}$ correspond to the linear and second- and third-order non-linear optical susceptibilities, respectively. The direct refractive index $n(\lambda)$ could be estimated as listed below:

$$n(\lambda) = n_{\text{av}}(\lambda) + n_2(E^2), \quad (20)$$

$n(\lambda)$ is ascertained as $n_{\text{av}}(\lambda) \gg n_2(\lambda)$, $n(\lambda) = n_{\text{av}}(\lambda)$ and (E^2) is mean square electric field values.

The $\chi^{(1)}$ values of these parameters are carried out utilizing the following equations [57, 58]:

$$\chi^{(1)} = \frac{h_{\text{av}}^2 - 1}{4\pi}. \quad (21)$$

The non-linear optical susceptibility of third-order ($\chi^{(3)}$) has been implied from the equation [59]

$$\chi^{(3)} = A(\chi^{(1)})^4, \quad (22)$$

where A is a constant provided as $1.7 \cdot 10^{-10}$ esu [57, 58].

Depending on the earlier aspects, the higher-order refractive index could be deduced as reported by Miller's principle [60, 61]:

$$n_2 = \frac{12\pi\chi^{(3)}}{n_{\text{AV}}}. \quad (23)$$

The estimated $\chi^{(1)}$, $\chi^{(3)}$, and n_2 values of $\text{Li}_2\text{Ge}_4\text{O}_9-x\text{Mn}^{4+}$ GCs samples with different Mn^{4+} ion content are estimated

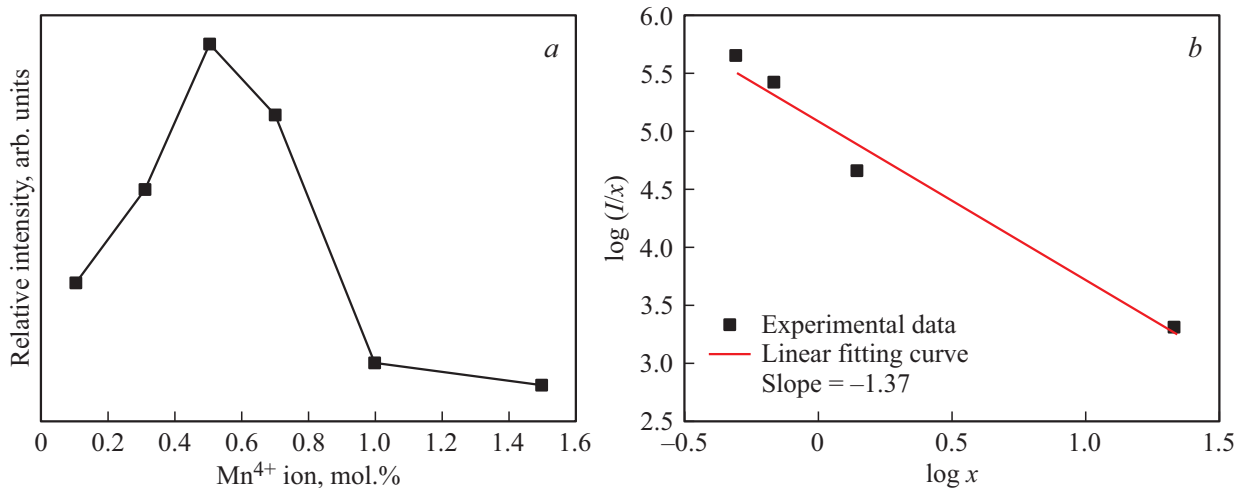


Figure 13. (a) Normalized integrated intensity of GC samples PL dependence on Mn^{4+} contents. (b) The $\log(I/x)$ dependence on $\log(x)$.

by using Eqs (21)–(23) and illustrated in Table 2. From the listed values, it is apparent that the $\chi^{(1)}$ and $\chi^{(3)}$ increase with increasing the Mn^{4+} additive. This improvement may be because of the GCs molecules' aligned chains in the stimulated electrical field. The refractive index with higher-order (n_2) had an Mn^{4+} ion=concentration dependence since their values enhance with concentration. The n_2 value increased from $3.68 \cdot 10^{-11}$ to $10.619 \cdot 10^{-11}$ esu as the concentration increased from 0.1 up to 1.5%.

Fig. 12 describes the GCs emission spectra doped with different Mn^{4+} contents. Under 325-nm excitation wavelength, the PL spectra display a narrow red band at 668-nm wavelength ascribed to the Mn^{4+} spin-forbidden ${}^4E_g \rightarrow {}^4A_{2g}$ transition [13, 62, 63]. By increasing the Mn^{4+} concentration, the emission spectra shape remain unaffected; nevertheless, a concentration quenching behavior is observed at Mn^{4+} concentration higher than 0.5 mol.% (Fig. 12), which is commonly verified by the energy migration among nearest Mn^{4+} ions that eventually results in the dissipation of the excitation energy as heat [11]. In addition, for comparison, the emission spectra of the G-xMn^{2+} samples were presented (inset of Fig. 12). The PL spectra of G show a broad red band extended from 500 to 750 nm that belongs to the spin-forbidden $\text{Mn}^{2+}(\text{d}^5) {}^4T_{1g}(\text{G}) \rightarrow {}^6A_{1g}(\text{S})$ transition which occupies the host glass octahedral coordination sites. $\text{Mn}^{2+}(\text{d}^5)$ takes the octahedral coordination sites in the host glass [64,65].

For more investigation to the intensity diminished by growing the Mn^{4+} contents, the two nearest Mn^{4+} ions critical distance (R_c) was established based on Blasse's equation, Eq. (24) [66]:

$$R_c \approx 2 \left(\frac{3V}{4\pi X_c N} \right)^{1/3}. \quad (24)$$

Accordingly, the value of R_c is determined to be 3.9 Å. Herein the possibility of energy transfer over all Mn^{4+} ions

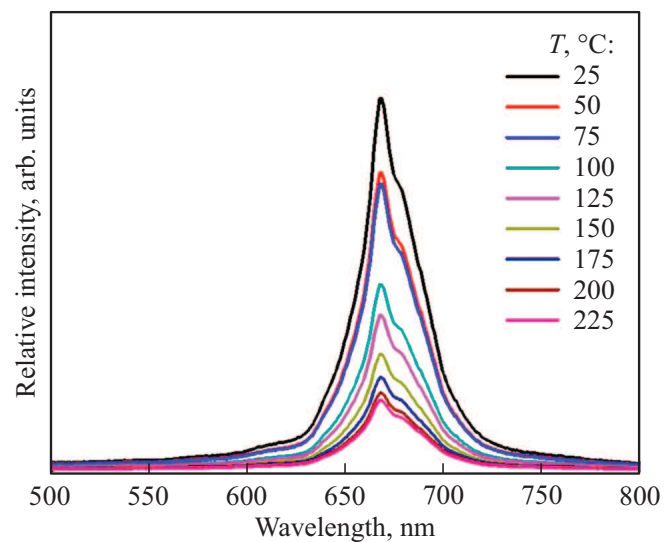


Figure 14. PL spectra dependence on temperatures (thermal stability) of GC-0.5.

via electronic exchange interactions is accepted since this process only performs at a short R_c , normally lower than 5 Å. However, for a small R_c value, the electric multipole interactions may also become dominating in energy transfer. As stated by Dexter's theory [67], the electric multiple interaction in energy transfer could be established by Eq. (25), the slope value ($-\theta/3$) of -1.37 with $\theta = 4.11$.

$$\frac{I}{X} = \frac{K}{1 + \beta(X)^{\theta/3}}. \quad (25)$$

Since the determined θ is approximately 6, we could suggest that the interactivity of the dipole-dipole mechanism is dominating for concentration quenching (see Fig. 13, a and b). Besides, the excitation spectra for $\text{Li}_2\text{Ge}_4\text{O}_9-0.5\text{Mn}^{4+}$

GCs monitored at 668 nm reveals one broadband centered at 335 nm originated from Mn–O charge transfer and two sharp peaks at 406 and 465 nm attributed to the ground state $^2A_{2g}$ transition to $^4T_{1g}$, $^2T_{2g}$, and $^4T_{2g}$ excited state of Mn^{4+} , respectively [6, 68, 69] (Fig. 12) which has good matches with the absorption spectra (Fig. 5, a). Finally, for more evidence about the thermal stability, under excitation at 460 nm, the PL was reported in response to the temperatures extended from 25 and 250°C. As described in Fig. 14, the thermal quenching is noted at temperatures up to 250°C for the GCs sample. Whereas the GC sample's emission rate is reduced by just 22 percent at 250°C. Besides, the GCs samples stay stable after reaching 250°C temperature, while the traditional polymer-glued phosphor operated in regular WLEDs will suffer supreme degradation at that elevated temperature. This outcome indicates that a crystalline host in the current system is favorable for stabilizing the emission of Mn^{4+} .

4. Conclusion

Mn^{4+} -ions-doped $Li_2Ge_4O_9$ glass-ceramic has been successfully fabricated via the thermal treatment of glass matrix ($80GeO_2-20Li_2O-xMn^{2+}$ in mol.%, $x = 0.1, 0.3, 0.5, 0.7, 1.0$ and 1.5). The creation of a $Li_2Ge_4O_9$ nanocrystalline precipitated through the glass matrix was verified by X-ray diffraction (XRD). The crystal size of the formed $Li_2Ge_4O_9$ crystals observed in the TEM illustration demonstrates a strong agreement with the predicted XRD pattern by introducing the Scherrer equation and the Williamson–Hall approach. The EPR measurement of the GC sample confirms the successful transformation from Mn^{2+} to Mn^{4+} , which dictates the change in optical properties by crystallization of the glass. By applying the Wemple–DiDomenico single-oscillator model, the refractive index n dispersion was analyzed, and the dispersion parameters (E_o and E_d) were calculated. The red shift of the direct optical bandgap from 3.81 to 2.55 eV is observed by increasing the Mn^{4+} concentration. The emission spectra of the GCs exhibit a narrow emission band centered at 668 nm belonging to the $3d^3$ electrons spin-forbidden $^4E_g \rightarrow ^4A_{2g}$ transition of Mn^{4+} . Also, the thermal quenching of the photoluminescence of the GC sample is notably reduced as compared with that of the glass samples. The preparation method exposed herein for the synthesis of Mn^{4+} -doped GCs might be prevailing for the production of identical luminescent ceramics following the glass's devitrification which implies potential application in advanced solid-state lighting in the future.

Acknowledgments

The authors extend their appreciation to the Research Center for Advanced Materials Science (RCAMS), King Khalid University, Saudi Arabia, for funding this work under grant number RCAMS/KKU/005-21.

Conflict of interests

The authors declare that they have no conflict of interests.

References

- [1] R. Suzuki, J. Kunitomo, Y. Takahashi, K. Nakamura, M. Osada, N. Terakado, and T. Fujiwara. *J. Ceram. Soc. Jpn* **123**, 1441, 888 (2015).
- [2] H. Masai, T. Yanagida, Y. Fujimoto, M. Koshimizu, and T. Yoko. *Appl. Phys. Lett.* **101**, 19, 191906 (2012).
- [3] P.F. Smet, A.B. Parmentier, and D. Poelman. *J. Electrochem. Soc.* **158**, 6, R37 (2011).
- [4] Y. Takahashi, K. Kitamura, N. Iyi, and S. Inoue. *Appl. Phys. Lett.* **88**, 15, 151903 (2006).
- [5] M. You, J. Xu, Z. Zhang, and Y. Zhou. *Ceram. Int.* **40**, 10, 16189 (2014).
- [6] B. Wang, H. Lin, J. Xu, H. Chen, and Y. Wang. *ACS Appl. Mater. Interfaces* **6**, 24, 22905 (2014).
- [7] S. Okamoto and H. Yamamoto. *J. Electrochem. Soc.* **157**, 3, J159 (2010).
- [8] Y. Zhang, S. Hu, Y. Liu, Z. Wang, G. Zhou, and S. Wang. *Ceram. Int.* **44**, 18, 23259 (2018).
- [9] R. Cao, J. Huang, X. Ceng, Z. Luo, W. Ruan, and Q. Hu. *Ceram. Int.* **42**, 11, 13296 (2016).
- [10] M. Peng, X. Yin, P.A. Tanner, M. Brik, and P. Li. *Chem. Mater.* **27**, 8, 2938 (2015).
- [11] X. Ding, G. Zhu, W. Geng, Q. Wang, and Y. Wang. *Inorganic Chem.* **55**, 1, 154 (2015).
- [12] W. Lü, W. Lv, Q. Zhao, M. Jiao, B. Shao, and H. You. *Inorganic Chem.* **53**, 22, 11985 (2014).
- [13] L. Meng, L. Liang, and Y. Wen. *J. Mater. Sci.: Mater. Electron.* **25**, 6, 2676 (2014).
- [14] S. Liang, M. Shang, H. Lian, K. Li, Y. Zhang, and J. Lin. *J. Mater. Chem. C* **4**, 26, 6409 (2016).
- [15] H. Zhang, H. Zhang, J. Zhuang, H. Dong, Y. Zhu, X. Ye, Y. Liu, and B. Lei. *Ceram. Int.* **42**, 11, 13011 (2016).
- [16] I. Morad, X. Liu, and J. Qiu. *J. Am. Ceram. Soc.* **102**, 10, 5843 (2019).
- [17] Y. Takahashi, J. Kunitomo, T. Miyazaki, M. Osada, and T. Fujiwara. *J. Appl. Phys.* **114**, 3, 033512 (2013).
- [18] J. Kunitomo, R. Suzuki, Y. Takahashi, T. Miyazaki, N. Terakado, and T. Fujiwara. *J. Ceram. Soc. Jpn* **122**, 1428, 725 (2014).
- [19] K. Omel'chenko, O. Khmelenko, T. Panchenko, and M. Volnyanskii. *Phys. Solid State* **56**, 4, 751 (2014).
- [20] A. Alias, T.I.T. Kudin, Z.M. Zabidi, M.K. Harun, A.M.M. Ali, and M.F. Yahya. *Adv. Mater. Res., Trans Tech Publ* **652–654**, 532 (2013).
- [21] M. El-Desoky. *J. Non-Crystal. Solids* **351**, 37-39, 3139 (2005).
- [22] I. Morad, H.E. Ali, M. Wasfy, A. Mansour, and M. El-Desoky. *Vacuum* **181**, 109735 (2020).
- [23] R. Apetz and M.P.B. Van Bruggen. *J. Am. Ceram. Soc.* **86**, 3, 480 (2003).
- [24] M. Saleem, L. Fang, H. Ruan, F. Wu, Q. Huang, C. Xu, and C. Kong. *Int. J. Phys. Sci.* **7**, 23, 2971 (2012).
- [25] C. Suryanarayana and N. Grant. *Practical Approach: X-Ray Diffraction. A Practical Approach.* Plenum Press, N. Y. (1998).
- [26] P. Bindu and S. Thomas. *J. Theor. Appl. Phys.* **8**, 4, 123 (2014).

- [27] T. Pandiyarajan and B. Karthikeyan. *J. Nanopart. Res.* **14**, 1, 647 (2012).
- [28] M. Volnianskii, M. Trubitsyn, and O. Bibikova. *Ferroelectrics* **443**, 1, 16 (2013).
- [29] H. Völlenkle, A. Wittmann, and H. Nowotny. *Monatshefte f. Chemie / Chemical Monthly* **100**, 1, 79 (1969).
- [30] I. Prakash, B. Babu, C.V. Reddy, P.N. Murty, Y. Reddy, P.S. Rao, and R. Ravikumar. *Physica B* **406**, 17, 3295 (2011).
- [31] S.K. Gupta, R. Kadam, R. Gupta, M. Sahu, and V. Natarajan. *Mater. Chem. Phys.* **145**, 1-2, 162 (2014).
- [32] V. Vazhenin, A. Potapov, V. Guseva, and M.Y. Artyomov. *Phys. Solid State* **52**, 3, 515 (2010).
- [33] Y. Zhang, S. Hu, Y. Liu, Z. Wang, W. Ying, G. Zhou, and S. Wang. *J. Eur. Ceram. Soc.* **39**, 2-3, 584 (2019).
- [34] R. Rakhimov, A. Wilkerson, G. Loutts, M. Noginova, N. Noginova, W. Lindsay, and H. Ries. *Solid State Commun.* **108**, 8, 549 (1998).
- [35] C. Ming, H. Liu, F. Song, X. Ren, L. An, Y. Hao, and G. Wang. *Current Appl. Phys.* **13**, 6, 1109 (2013).
- [36] T. Erdem and H.V. Demir. *Nature Photon.* **5**, 3, 126 (2011).
- [37] O. Dymshits, M. Shepilov, and A. Zhilin. *MRS Bull.* **42**, 3, 200 (2017).
- [38] J.L. Pankove. *Optical processes in semiconductors*. Courier Corporation (1975).
- [39] F. Urbach. *Phys. Rev.* **92**, 5, 1324 (1953).
- [40] K. Subrahmanyam and M. Salagram. *Opt. Mater.* **15**, 3, 181 (2000).
- [41] S. Rani, S. Sanghi, A. Agarwal, and V. Seth. *Spectrochim. Acta A* **74**, 3, 673 (2009).
- [42] N. Shah, J. Ray, V. Kheraj, M. Desai, C. Panchal, and B. Rehani. *J. Mater. Sci.* **44**, 1, 316 (2009).
- [43] S. Wemple and M. DiDomenico Jr. *Phys. Rev. B* **3**, 14, 1338 (1971).
- [44] H.S. Shaaker, W.A. Hussain, and H.A. Badran. *Adv. Appl. Sci. Res.* **3**, 5, 2940 (2012).
- [45] I. Saini, J. Rozra, N. Chandak, S. Aggarwal, P.K. Sharma, and A. Sharma. *Mater. Chem. Phys.* **139**, 2-3, 802 (2013).
- [46] I. Morad, A. Alshehri, A. Mansour, M. Wasfy, and M. El-Desoky. *Physica B* **597**, 412415 (2020).
- [47] T. Moss. *Phys. Status Solidi B* **131**, 2, 415 (1985).
- [48] V. Gupta and N. Ravindra. *Phys. Status Solidi B* **100**, 2, 715 (1980).
- [49] N.M. Ravindra, S. Auluck, and V.K. Srivastava. *Phys. Status Solidi B* **93**, 2, K155 (1979).
- [50] R. Reddy, K.R. Gopal, K. Narasimhulu, L.S.S. Reddy, K.R. Kumar, G. Balakrishnaiah, and M.R. Kumar. *J. Alloys Comp.* **473**, 1-2, 28 (2009).
- [51] P. Hervé and L. Vandamme. *Infrared Phys. Technol.* **35**, 4, 609 (1994).
- [52] V. Kumar and J. Singh. *Indian J. Pure & Appl. Phys.* **48**, 571 (2010).
- [53] Y. Akaltun, M.A. Yildirim, A. Ateş, and M. Yildirim. *Opt. Commun.* **284**, 9, 2307 (2011).
<https://doi.org/10.1016/j.optcom.2010.12.094>
- [54] P.N. Prasad and D.R. Ulrich. *Nonlinear optical and electroactive polymers*. Plenum Press, N.Y. (2012).
- [55] M.S. Reddy, K.R. Reddy, B. Naidu, and P. Reddy. *Opt. Mater.* **4**, 6, 787 (1995).
- [56] M. Frumar, J. Jedelský, B. Frumarova, T. Wagner, and M. Hrdlička. *J. Non-Crystal. Solids* **326-327**, 399 (2003).
- [57] V. Ganesh, I. Yahia, S. AlFaify, and M. Shakir. *J. Phys. Chem. Solids* **100**, 115 (2017).
- [58] H. Tichá and L. Tichý. *J. Optoelectron. Adv. Mater.* **4**, 2, 381 (2002).
- [59] C.C. Wang. *Phys. Rev. B* **2**, 6, 2045 (1970).
- [60] T.A. Hamdalla, S.M. Selim, A.K. Mohamed, and M.E. Mahmoud. *Opt. Mater.* **95**, 109215 (2019).
- [61] L. Tichý, H. Tichá, P. Nagels, R. Callaerts, R. Mertens, and M. Vlček. *Mater. Lett.* **39**, 2, 122 (1999).
- [62] R. Cao, Y. Jiao, X. Wang, X. Ouyang, H. Wan, T. Chen, G. Zheng, and S. Xie. *Adv. Powder Technol.* **31**, 9, 4045 (2020).
- [63] R. Cao, W. Zhang, T. Chen, Y. Zheng, H. Ao, Z. Luo, S. Xie, and H. Wan. *Mater. Res. Bull.* **137**, 111200 (2021).
- [64] A. Winterstein, H. Akamatsu, D. Möncke, K. Tanaka, M. Schmidt, and L. Wondraczek. *Opt. Mater. Express* **3**, 2, 184 (2013).
- [65] Z. Zou, J. Wu, H. Xu, J. Zhang, Z. Ci, and Y. Wang. *J. Mater. Chem. C* **3**, 31, 8030 (2015).
- [66] G. Blasse. *J. Solid State Chem.* **62**, 2, 207 (1986).
- [67] D.L. Dexter and J.H. Schulman. *J. Chem. Phys.* **22**, 6, 1063 (1954).
- [68] A. Fu, A. Guan, D. Yu, S. Xia, F. Gao, X. Zhang, L. Zhou, Y. Li, and R. Li. *Mater. Res. Bull.* **88**, 258 (2017).
- [69] B. Wang, H. Lin, F. Huang, J. Xu, H. Chen, Z. Lin, and Y. Wang. *Chem. Mater.* **28**, 10, 3515 (2016).